Climatological evaporation seasonality in the northern Red Sea

Gidon Eshel[1] and Nicholas Heavens[2,3]

[1] The dynamic and thermodynamic processes that underlie the exceptionally high evaporation over the northern Red Sea are examined. Through a combination of data analysis and a simple numerical model we show that the key boundary layer dehumidifier is ageostrophic cross-channel sea breezes. This circulation develops semidiurnally in response to thermal gradients across the Red Sea's coasts because of disparate land-ocean heat capacities. During the summer day the thermally induced high-pressure center over the Red Sea axis results in near-surface flows from the Red Sea toward the neighboring deserts. The strong divergence associated with these flows is maximized along the Red Sea axis and is accompanied by strong subsidence that suppresses boundary layer relative humidity by both reducing specific humidity and increasing temperatures. Because the summer nighttime reversed thermal gradients are smaller in magnitude, the daytime circulation dominates over the nighttime in summer and thus dominates over the daily and seasonal means. Following similar reasoning, we also devise a winter dehumidifier. We conclude by advancing a simple means of estimating Red Sea evaporation under diverse paleoinsolation regimes, and we show small but clear evaporation changes during the course of the Holocene. Our estimates represent lower bounds, and we plan to refine them in follow-up work.

1. Introduction

[2] Recently, the Red Sea has been used to derive powerful constraints on the fundamental problem of global sea level throughout most of the last glacial cycle [*Thunell et al.*, 1988; *Rohling*, 1994; *Rohling et al.*, 1998; *Arz et al.*, 2003, 2007; *Siddall et al.*, 2003; *Sirocko*, 2003]. Key to estimating the uncertainty range of these authors' method is northern Red Sea (NRS) evaporation rate. Yet, the physics governing the seasonality of climatological evaporation in the northern Red Sea (roughly north of 24°N) are neither fully understood nor extensively studied. Improving our understanding of the physics and dynamics underlying climatological seasonal evaporation in the NRS is the focus of this paper.

[3] Further progress in the global sea level problem, as well as other key local and global, past, modern and future, problems, hinges on better understanding of those physics. First, evaporation over the NRS is a crucial element of the Red Sea oceanic circulation [e.g., *Cember*, 1988, 1989; *Eshel and Naik*, 1997; *Eshel et al.*, 2000]. Consequently, better understanding of NRS evaporation is likely to improve understanding of the Red Sea circulation. Second, the central element of the setting we address in this paper is land-ocean thermal contrasts, in particular seasonally and

diurnally varying thermal gradients across the coast. As Figure 1 shows, such coastal contrasts are globally ubiquitous. In turn, thermal contrasts, and the related along- and cross-shore winds, are the primary driving force for such important coastal phenomena as (irrotational and rotational) coastal upwelling and high oceanic biological productivity, enhanced orographic precipitation and the resultant elevated vegetation cover of global coastal ranges, increased riverine input into the coastal ocean, high sedimentation rates characteristic of continental shelves, among others. Thus the current paper's main objective, better understanding of atmospheric dynamics and thermodynamics that arise near a coast because of thermal gradients, is pertinent to modern and paleocoastal regions both in the NRS and worldwide.

[4] While our motivation is in part global, the special simplifications permitted by the unique geography of the NRS, virtually no precipitation and vegetation and exceptionally high land-sea thermal contrasts that overwhelm all other physical processes [*Morcos*, 1970], simplify the modeling and make the location ideal for developing and testing a specific yet generalizable conceptual and numerical model of air−sea−land interactions near a coast.

## 2. Some Characteristics of the Northern Red Sea Boundary Layer

2.1. Evaporation Variability

[5] Because evaporation measurements are extremely rare, evaporation is nearly universally estimated using a notoriously imperfect bulk formula [e.g., *Sobel*, 2003]. This has also been true for Red Sea evaporation estimates [*Tragou et al.*, 1999; *Sofianos et al.*, 2002; *Smeed*, 2004]. This paper is no exception, using the bulk-based standard

[1]Division of Science, Mathematics and Computing, Bard College at Simon's Rock, Great Barrington, Massachusetts, USA.

[2]Department of Geophysical Sciences, University of Chicago, Chicago, Illinois, USA.

[3]Now at Division of Geological and Planetary Sciences, California Institute of Technology, Pasadena, California, USA.
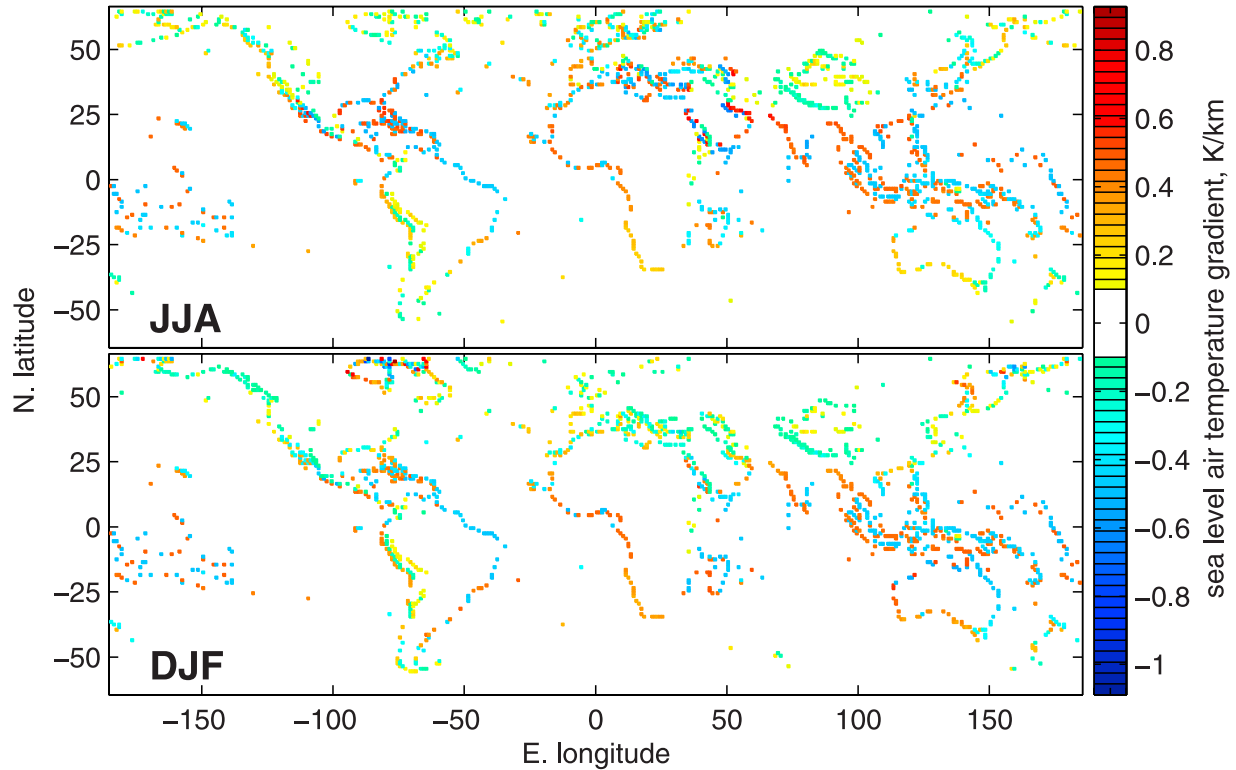
Figure 1. Climatological seasonal gradients of surface air temperature T_s. The field shown is $\partial_x T_s + \partial_y T_s$ in K km^{-1} on a $0.5° \times 0.5°$ spatial grid. Ocean and land T_s are taken from *da Silva et al.* [1994] and *Jones and Moberg* [2003], respectively. Grid points with $|\partial_x T_s + \partial_y T_s| \le 0.1$ K km^{-1} appear white irrespective of the actual value (i.e., colored grid points satisfy $|\partial_x T_s + \partial_y T_s| > 0.1$ K km^{-1}). Coast lines are not explicitly plotted.

estimates of *da Silva et al.* [1994]. With this limitation in mind, NRS evaporation (spatial mean annual average of the seven $1° \times 1°$ ocean grid points within $33°–38°$E, $24°–28°$N) is estimated to be 2.02 m yr^{-1}. With the tropics' mean and standard deviation of 1.46 and 0.25 m yr^{-1} (computed over the 15,934 $1° \times 1°$ ocean grid points between 30°S and 30°N), the NRS value is ~2.2 standard deviations above the tropics mean. In fact, of the 15,934 tropical ocean grid points, only 51, or ~0.3%, have evaporation rates higher than those in the NRS. That is, by any reasonable measure, NRS evaporation is outstandingly high.

[6] The spatial mean [*da Silva et al.*, 1994] NRS evaporation is maximized during winter (December–February, or DJF; 143% of the annual mean) and minimized during summer (June–August, or JJA; 66% of the annual mean), with intermediate values in the transition seasons. Figures 2a and 2b show that both statements are also true locally at 24°N and 27°N, where the horizontal axis is the latitude along the Red Sea axis given by longitude = $42.3° − 7.6°$(latitude − $14.5°)/12.5°$, which simply reflects the Red Sea geometry. Figures 2c–2e show that at all times, evaporation is maximum in the northernmost NRS, decreasing to the south.

2.2. Previously Proposed Mechanisms of Northern Red Sea Evaporation Variability

[7] Investigating monthly mean anomalous ocean NRS surface density, *Eshel et al.* [2000] showed that low-level subsidence variability explains a large fraction of the observed ocean surface density fluctuations, interpreted as reflecting evaporation intensity. In turn, they showed that the subsidence can be diagnostically understood in the context of the heat equation. On the basis of scale analysis, they showed that the vertical advective heat flux divergence associated with the subsidence, $-\omega\partial_p\theta$ where p is pressure, $\omega \equiv dp/dt$ is subsidence in pressure coordinate and θ is potential temperature, is closely balanced by its lateral counterpart, $-u\partial_x\theta − v\partial_y\theta$, where u (v) is eastward (northward) wind. Because *Eshel et al.* [2000] addressed monthly mean anomalies (deviations of the mean of a given month from that calendar month's long-term climatology), their proposed mechanism may or may not apply to the subject of inquiry here, the climatologies themselves.

[8] If the findings of *Eshel et al.* [2000] regarding the relationship between monthly mean anomalous subsidence and evaporation apply also to the climatologies of these fields, the seasonal climatologies of the two fields must vary in concert. However, Figure 2 shows that the seasonalities of the two fields are anticorrelated. Figures 2a and 2f (Figures 2b and 2g) show monthly mean mid-channel climatological evaporation and subsidence, respectively, at 24°N (27°N). Evaporation and subsidence extrema clearly occur at different seasons in either location. In the northernmost NRS, where evaporation is maximized (Figures 2c–2e), seasonal maximum evaporation occurs in
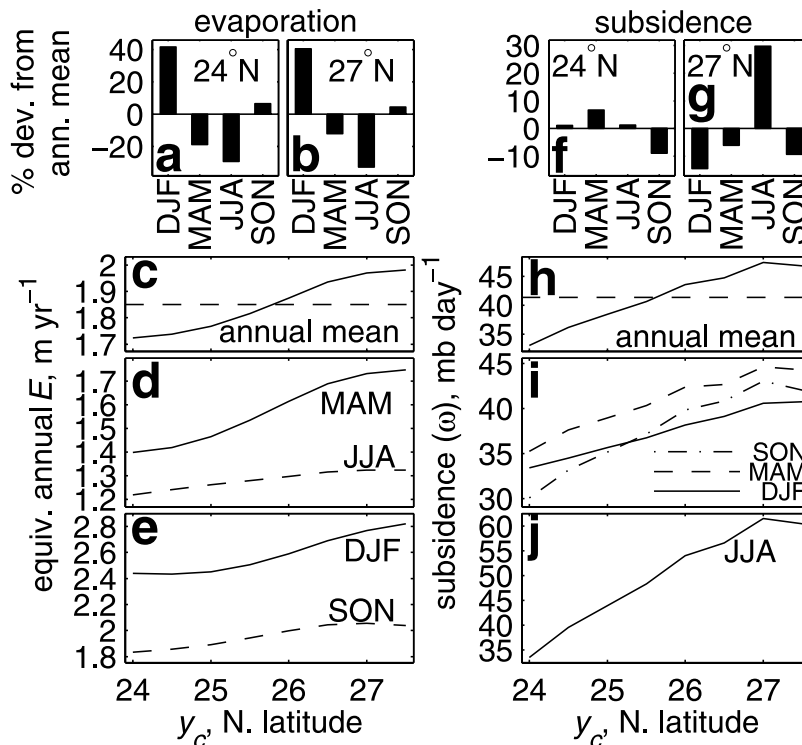
Figure 2. Monthly mean climatological (a–e) evaporation [from *da Silva et al.*, 1994] and (f–j) subsidence [from *Kalnay et al.*, 1996] along the central axis of the NRS. Figures 2a and 2b show the seasonal evaporation variability at 24°N and 27°N, respectively. Figure 2c shows the annual mean evaporation, with the spatial mean annual mean evaporation over the domain given by the dashed line. Figures 2d and 2e show the seasonal evaporation estimates, expressed as the equivalent annual total flux. The subsidence plots (Figures 2f–2j) follow the same convention as Figures 2a–2e, except that Figures 2i and 2j show three and one season, respectively.

winter (DJF, Figure 2b), the season of subsidence minimum (Figure 2g). Conversely, 27°N evaporation minimum, JJA (Figure 2b), is the time of maximum subsidence (Figure 2g). Evaporation and subsidence at 27°N during the two transition seasons appear largely unrelated (Figures 2b and 2g). Evaporation and subsidence are also seasonally unrelated at 24°N (Figures 2a and 2f). Further, while both evaporation and subsidence maximize in the north and decrease down the channel (Figures 2c–2e and Figures 2h–2j, respectively), their relative down channel changes are clearly distinct. While seasonal relative evaporation is rather uniform between 24°N and 27°N (see the similarity of Figures 2a and 2b), relative subsidence is very different in the two locations (Figures 2f and 2g).

[9] Combining the spatial and temporal information of Figure 2, Figure 3 shows NRS spatial averages of absolute subsidence and evaporation and further demonstrates the anticorrelation between climatological seasonal NRS evaporation and subsidence. Jointly, Figures 2 and 3 show that climatological NRS evaporation and subsidence are seasonally anticorrelated. This clearly demonstrates the inconsistency of NRS observations with the notion that climatological seasonality of subsidence causes that of evaporation, and emphasizes the presence of an alternative

mechanism(s) linking subsidence and evaporation climatologies and resulting in their anticorrelation.

3. Analysis of NRS Monthly Mean Moisture Budget

[10] We begin our search for alternative subsidence–evaporation dynamical linkages by analyzing the NRS moisture budget. Denoting seasonal means by overbars, this budget is given locally by

$$\frac{\partial \overline{q}}{\partial t} \approx 0 = -\overline{\mathbf{V}}_2 \cdot \nabla_2 \overline{q} - \overline{\omega}\frac{\partial \overline{q}}{\partial p} - \nabla_3 \cdot \left(\overline{\mathbf{V}'_3 q}\right) + \frac{\overline{E\rho_w}}{h\rho_a} \quad (1)$$

where we assume that on seasonal scales the tendency approximately vanishes. In (1), $\mathbf{V}_2 \equiv (u\ v)^T$ and $\mathbf{V}_3 \equiv (u\ v\ \omega)^T$ are the lateral and full (three-dimensional) flow fields, and $\nabla_2 \equiv (\partial_x\ \partial_y)^T$ and $\nabla_3 \equiv (\partial_x\ \partial_y\ \partial_p)^T$ are the lateral and full (three-dimensional) nabla operators. The "Reynolds" term $-\nabla_3 \cdot (\overline{\mathbf{V}'_3 q})$ denotes boundary layer (BL) moistening by correlations of moisture and flow on small temporal and spatial scales. Note that it does not conform to the traditional Reynolds formulation, which includes only fluctuations. Consequently, we use the term in quotes, only as a shorthand. In the context of data derived from the
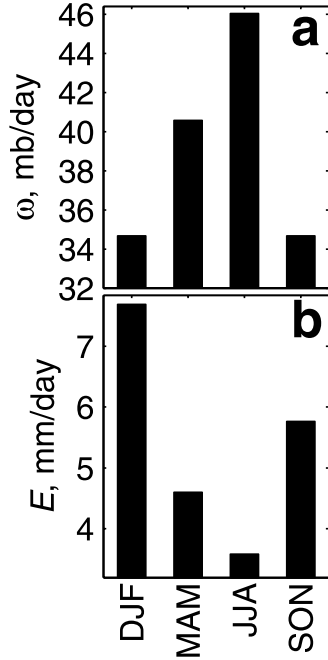
Figure 3. Monthly and spatial mean NRS climatological (a) subsidence [from *Kalnay et al.*, 1996] and (b) and evaporation [from *da Silva et al.*, 1994]. Figure 3a shows the average of the three mostly oceanic reanalysis 2.5° × 2.5° grid points in the NRS, centered at 25°N, 35°E; 25°N, 37.5°E; and 27.5°N, 35°E. Figure 3b shows the average of the five 1° × 1° oceanic grid points contained in the range 33°–37°E, 25°–28°N.

coarse resolution reanalysis [*Kalnay et al.*, 1996], for example, the term may represent moistening by subgrid-scale correlations of local flow and moisture variability, or local deviations from the respective grid cell means.

[11] The rightmost term represents BL moistening by sea surface evaporation. We estimate its magnitude for summer and winter using $\rho_w/\rho_a \sim 10^3$ and the representative summer (winter) values $E \sim 1.3$ m yr^{-1} ($E \sim 2.9$ m yr^{-1}). These E estimates are derived from the annual mean of 2 m yr^{-1} with 66% (143%) of the annual mean in JJA (DJF). Finally, we set $h \sim 400$ m ($h \sim 300$ m) in summer (winter), based on BL depth calculated using 6 hourly NRS reanalysis data and the bulk Richardson number method described in *Eshel and Bernstein* [2006] following *Deardroff* [1972], *Holstlag and Moeng* [1991], *Vogelezang and Holtslag* [1996] and the National Center for Atmospheric Research's CAM2 Community Atmospheric Model (W. D. Collins et al., Description of the NCAR Community Atmosphere Model (CAM2), especially their equation (4.459), 2003, available at http://www.ccsm.ucar.edu/models/atm-cam/docs/description/index.html). Using the above characteristic values, in summer

$$\frac{\overline{E\rho_w}}{h\rho_a} \approx \frac{1.3 \text{ m yr}^{-1} \cdot 10^3}{400 \text{ m}} \approx 9 \ \frac{\text{g}}{\text{kg} \cdot \text{d}}, \quad (2)$$

while in winter

$$\frac{\overline{E\rho_w}}{h\rho_a} \approx \frac{2.9 \text{ m yr}^{-1} \cdot 10^3}{250 \text{ m}} \approx 26 \ \frac{\text{g}}{\text{kg} \cdot \text{d}}. \quad (3)$$

We next explore various terms in (1) potentially capable of balancing the evaporative moistening.

[12] We have pointed out earlier that monthly mean NRS subsidence is not positively correlated with evaporation as would be required if subsidence variability were a prime modulator of evaporation. A corollary of this is that an approximation to equation (1) in which monthly mean subsidence balances BL evaporative moistening,

$$\overline{\omega}\frac{\partial\overline{q}}{\partial p} \approx \frac{\overline{E\rho_w}}{h\rho_a}, \quad (4)$$

should not work. To verify this, we recast (4) as

$$\frac{\overline{E\rho_w}}{h\rho_a} \approx \overline{\omega}_p \frac{\overline{q}_p - \overline{q}_o}{p - p_o} \quad (5)$$

where the subscript o denotes surface values, and use the reanalysis to calculate seasonal climatologies of (5) for the NRS over 600 mbar $\leq p \leq$ 1000 mbar. These calculations are shown in Figures 4a and 4c; the left side of (5) is larger or, in winter, much larger, than the right, indicating that equation (5) does not represent a viable approximation. Alternatively, we can rearrange equation (5),

$$\hat{\omega}_p = \frac{\overline{E\rho_w}}{h\rho_a}\left(\frac{p - p_o}{\overline{q}_p - \overline{q}_o}\right) \quad (6)$$

to obtain $\hat{\omega}_p$, the subsidence needed at p, given the approximate $\partial_p q$ there, in order to balance equation (5). These calculations, shown in Figures 4b and 4d, indicate that in both seasons $\hat{\omega}_p \gg \omega$ at all considered p levels; while $\omega\partial_p q \sim$ O(1 g kg^{-1} d^{-1}), the evaporative term is O(10 g kg^{-1} d^{-1}). As predicted, equations (4) and (5) clearly fail, especially in winter, to represent an approximate balance anywhere in the lower troposphere; in the NRS, drying by monthly mean subsidence is far too weak (and sometimes of the wrong sign) to balance evaporative BL moistening.

[13] Another possibility is that evaporative BL moistening is balanced by monthly mean lateral advective moisture flux divergence,

$$\overline{\mathbf{V}}_2 \cdot \nabla_2\overline{q} \approx \frac{\overline{E\rho_w}}{h\rho_a}. \quad (7)$$

We compute monthly $\overline{\mathbf{V}}_2 \cdot \nabla_2\overline{q}$ over 1949–2006 and form the seasonal JJA and DJF climatologies reported in Figure 5. Since the summer values reported in Figure 5a are 1–2 g kg^{-1} d^{-1}, there is roughly an order of magnitude disparity between the left and right sides of equation (7) in summer. Further, north of ∼26.5°N, the central evaporation locus,
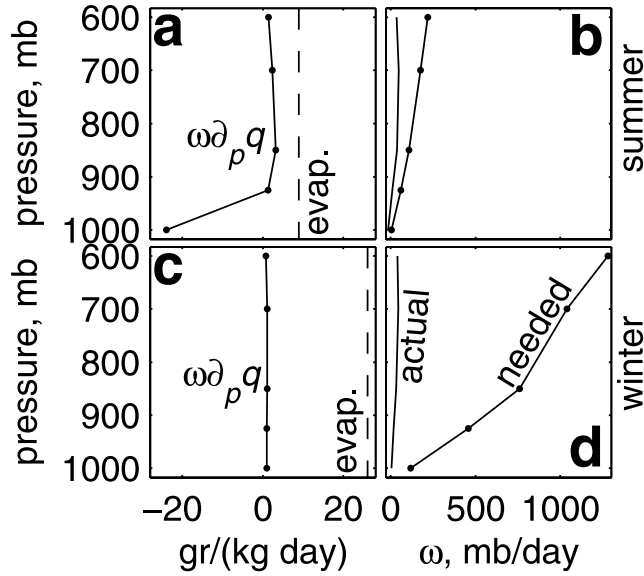
Figure 4. An attempt to approximate the full moisture budget according to equation (1), with drying by monthly mean subsidence balancing evaporative moistening. (a and c) Evaporative moistening, $\overline{E\rho_w/(\rho_a h)}$, shown by the dashed vertical line, and $\overline{\omega}\partial_p\overline{q}$ climatology, shown by the solid curve. Clearly, moisture flux divergence (the left-hand side of equation (1)) is too small, in both seasons, to balance evaporation (the right-hand side of equation (1)). (b and d) Actual reanalysis $\overline{\omega}$ (solid curve) as well as the subsidence needed at any level to balance evaporative moistening (equation (6), solid dotted curve). The needed subsidence far exceeds the actual monthly mean one at all levels.

even the sign of $\overline{\mathbf{V}}_2 \cdot \nabla_2\overline{q}$ in summer is inconsistent with equation (7), because advective moisture flux divergence actually further moistens the NRS BL there, i.e., further upsets the moisture balance. In winter (Figure 5b), $\overline{\mathbf{V}}_2 \cdot \nabla_2\overline{q} > 0$, as required by equation (7), but the right side of the equation is roughly 2 orders of magnitude smaller than the left. Clearly, equation (7) is invalid; something else must balance evaporative NRS BL moistening.

[14] Since we have exhausted all monthly, and grid cell, mean terms in equation (1) and found no term capable of balancing evaporative BL moistening, the leading order balance in equation (1) is most likely

$$\nabla_3 \cdot \left(\overline{\mathbf{V}'_3 q}\right) \approx \frac{\overline{E\rho_w}}{h\rho_a}, \tag{8}$$

drying by subgrid-scale processes balancing evaporative BL moistening.

4. A Proposed Meaning of the "Reynolds" Term

[15] Of the many processes potentially represented by $\nabla_3 \cdot \left(\overline{\mathbf{V}'_3 q}\right)$, we find diurnal ageostrophic cross-channel sea breeze flows the most compelling for NRS BL drying. Figures 6a and 6b show the east-west summer distribution of surface air temperature and its diurnal variability. Note that the *da Silva et al.* [1994] data are based on ship

observations alone and thus represent exclusively the oceanic setting.

[16] Mean maximum land temperatures (corresponding to daytime) near the NRS coasts is 38°–40°C in summer. While we have no direct information about the diurnal cycle of surface air temperatures over the NRS, it is considerably smaller than that over land. For example, useful high-frequency measurements from the Gulf of Aqaba, just north of the area of interest, are reported by *Genin et al.* [2002]. From Figures 1a and 1b of Genin et al., it can be estimated that the diurnal temperature amplitude over the ocean is $\sim$1–2 K for air temperature and less than that for SST in both summer and winter. This estimated $\pm$1.5 K air temperature range is shown in Figure 6 by vertical lines centered on the ocean points. However, compared with the surface temperature (T_s) range spanned by Figure 6 as
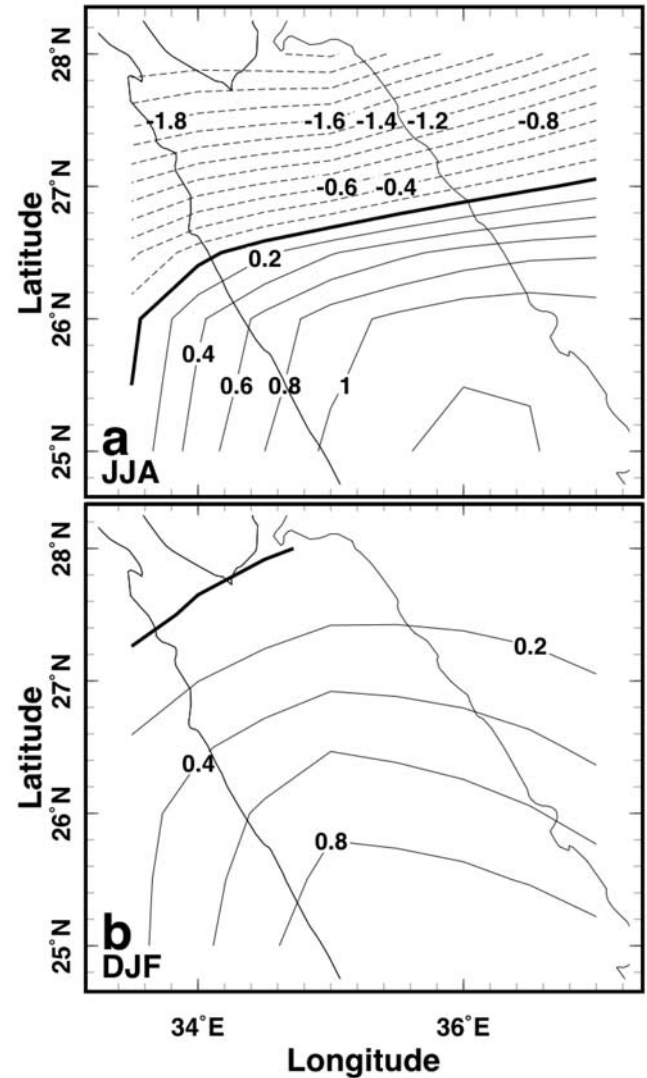
Figure 5. Climatological (a) summer (JJA) and (b) winter (DJF) drying in g kg^{-1} d^{-1} by monthly mean lateral advective moisture flux divergence, $u\partial_x q + v\partial_y q$, averaged vertically over 850–1000 mbar.
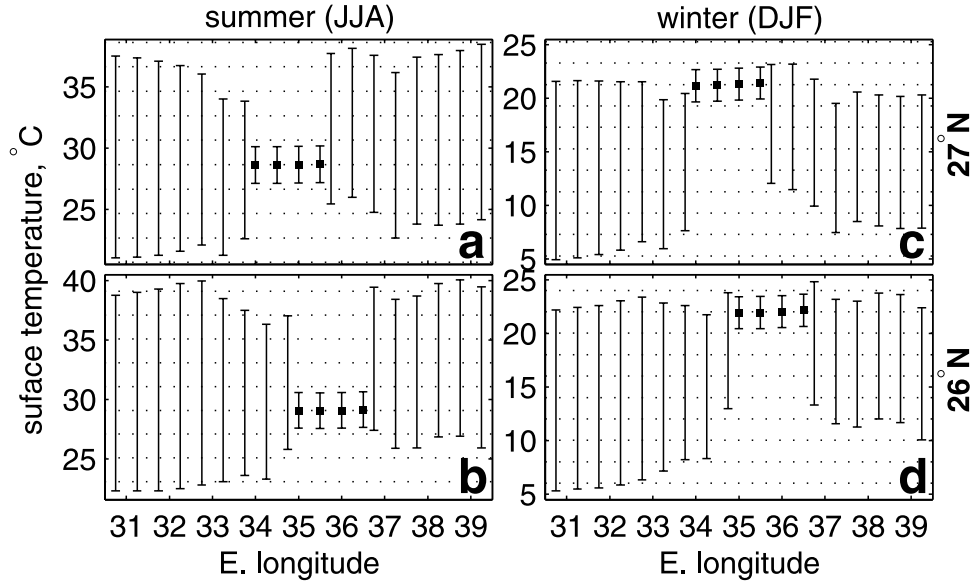
Figure 6. Climatological (a and b) summer (JJA) and (c and d) winter (DJF) surface air temperature along 27°N (Figures 6a and 6c) and 26°N (Figures 6b and 6d). Air temperatures over the ocean are shown with squares (four points per plot). Their diurnal variability [from *da Silva et al.*, 1994] is estimated at ±1.5 K (see text), shown by the bars crossing the four ocean points in each plot. For each land longitude, air temperature monthly mean maximum and minimum [from *New et al.*, 2000] span the height of the vertical bars (noted by the absence of squares). The horizontal dotted lines show increments of 2 K above and below the mean ocean temperature.

dictated by diurnal T_s variability over land, $\sim$22°–40°C ($\sim$5°–24°C) in summer (winter), the sea surface temperatures are weakly diurnally variable in both seasons. Thus in summer the maximum air temperature over the ocean during the day is at most 29°C, and the land-sea contrast is roughly +9 K. By comparison, mean summer minimum land temperatures (corresponding to nighttime) near the NRS coasts is $\sim$22°C while the air temperature over the ocean at night is $\sim$27°C, yielding a land-sea contrast of −5 K. Thus Figure 6 shows a summer landward warming (cooling) tendency away from the Red Sea axis during the day (night).

[17] In winter, $T_s^{ocean} \approx$ 23°C (21°C) and $T_s^{land} \approx$ 22°C (6°C) during the day (night). The approximate daytime (nighttime) winter land-sea temperature contrast is therefore −1 K (−15 K).

[18] These gradients are of course expected given the vastly different vertically integrated heat capacities of land and ocean. More importantly, they are likely to cause vigorous lateral exchanges by small-scale, high-frequency flows that are not explicitly represented by the monthly means on the reanalysis' coarse spatial grid. Since air humidity and temperature may vary laterally and vertically, the resultant sea breeze may play an important role in NRS thermodynamics. Estimating this role is the purpose of the following section.

5. A Simple Model of Cross-Channel Exchanges in the Northern Red Sea

[19] Consider an atmospheric layer shown schematically in Figure 7 spanning the troposphere's lowermost h = 900 m,

with an assumed uniform p_h = 925 mbar pressure at h. Assuming hydrostatics, the surface pressure is

$$p_s = p_h + \tilde{\rho}gh \qquad (9)$$

in which the vertical mean density of the layer is approximately

$$\tilde{\rho} \equiv \frac{1}{2}(\rho_s + \rho_h) = \frac{1}{2R}\left(\frac{p_s}{T_s} + \frac{p_h}{T_h}\right) \qquad (10)$$

(see below for the validity of the density linearity with height assumption), and the last stage involves invoking the ideal gas law for air, $p = \rho_a RT$, with R = 287 J kg^{-1} K^{-1} the dry air gas constant. Substituting equation (10) into equation (9),

$$p_s = p_h + \frac{gh}{2R}\left(\frac{p_s}{T_s} + \frac{p_h}{T_h}\right) \qquad (11)$$

where T_h and T_s are the temperatures at the layer's top and bottom. Expanding the right-hand side and rearranging, (11) becomes

$$p_s = p_h\left(\frac{T_s}{T_s + \tilde{\Gamma}h}\right)\left(\frac{2R(T_s + \Gamma h) + gh}{2RT_s - gh}\right) \qquad (12)$$

where Γ is the (assumed uniform) lapse rate. Because the NRS is dominated by subsidence and condensation is rarely realized, we set Γ = −8 K km^{-1}. Figure 8 shows the T_s
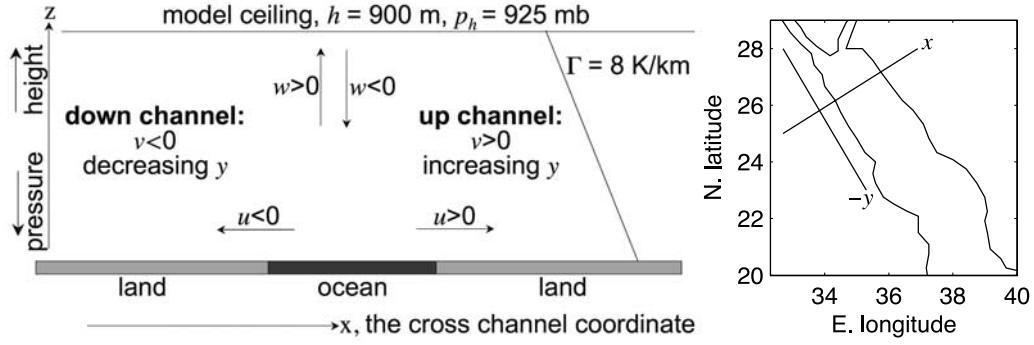
Figure 7. (left) Basic setup of the model described in the text. (right) A semirealistic application of the model geometry to that of the real Red Sea. The x and $-y$ directions are indicated. The corresponding velocity components are u and $-v$, respectively.

dependence of p_s and $\wp$ for our choice of $h = 900$ m, and suggests that approximation (10) is adequate.

[20] The pressure gradient vanishes at h, by construction (because p_h is fixed), attains its maximum at the surface, and varies very nearly linearly between the surface and h (see the near coincidence of the solid and dashed curves in Figure 8). Therefore the layer vertical mean pressure gradient can be approximated with great accuracy as the simple arithmetic mean of the pressure gradient at the surface and at h (the latter being zero),

$$\frac{1}{p_s - p_h} \int_{p_h}^{p_s} \left(-\frac{1}{\rho} \frac{\partial p}{\partial x} \right) dp \approx -\frac{1}{2\tilde{\rho}} \frac{\partial p_s}{\partial x}. \quad (13)$$

[21] As temperature decreases linearly with height according to Γ, the layer mean temperature is

$$\tilde{T} = \frac{1}{2}(T_s + T_h) = T_s + \frac{1}{2}\Gamma h. \quad (14)$$

Since Γ and h are both fixed, the layer mean temperature gradient and tendency are $\partial_x T_s$ and $\partial_t T_s$, respectively. The heat equation for the layer is therefore

$$\frac{\partial T_s}{\partial t} = -u \frac{\partial T_s}{\partial x} - w_h \frac{\theta_h}{h} + \kappa \frac{\partial^2 T_s}{\partial x^2} - \frac{1}{\tau}\left(T_s - T^*\right) \quad (15)$$

where $\tau^{-1} = 1$ hour. In (15), the second right-hand-side term accounts for subsidence heating, and the last right-hand-side term relaxes the surface temperature distribution toward a prescribed state, parameterizing the different response to solar heating of land and ocean because of their widely disparate heat capacities. Guided by the surface temperature observations discussed in section 3.1 (based on Figure 6),

$$
\begin{aligned}
T^*(x)_{\text{night}}^{\text{summer}} &= 300 \text{ K} - 5 \text{ K} \cdot \phi(x) \\
T^*(x)_{\text{d}}^{\text{summer}} &= 302 \text{ K} + 9 \text{ K} \cdot \phi(x) \\
T^*(x)_{\text{night}}^{\text{winter}} &= 294 \text{ K} - 15 \text{ K} \cdot \phi(x) \\
T^*(x)_{\text{d}}^{\text{winter}} &= 296 \text{ K} - 1 \text{ K} \cdot \phi(x)
\end{aligned}
\quad (16)
$$

where the spatial structure function (with x is expressed in km) is

$$\phi(x) = 1 + \frac{9}{20}\left[\tanh\left(\frac{x-120}{60}\right) - \tanh\left(\frac{x+120}{60}\right)\right]. \quad (17)$$

In (16), 302 and 300 K (296 and 294 K) are day and night summer (winter) base surface temperatures, and 9 and -5 K (-1 and -15 K) are the approximate respective day and night land-ocean temperature differences based on Figure 6. The structure function $\phi(x)$ and the resultant seasonal $T^*(x)$ are shown in Figure 9.

[22] The vertical transport term in equation (15) requires the subsidence and potential temperature at h, w_h, and θ_h. To
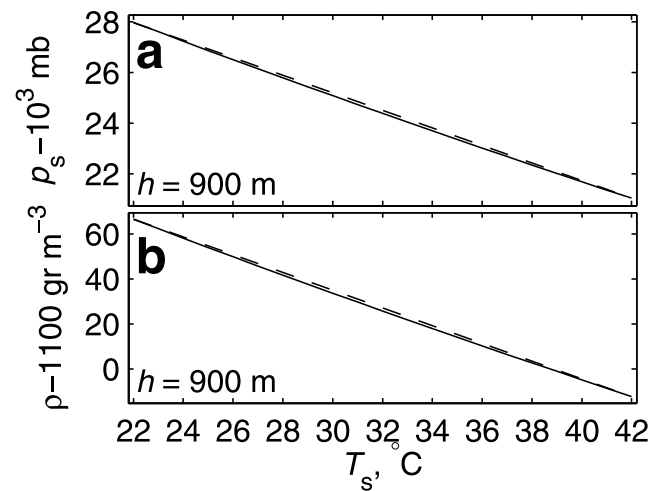
Figure 8. T_s dependence of the (a) surface pressure and (b) vertical mean density. The solid curves give the values using the full equation of state. The straight dashed lines connect the first ($T_s = 22°C$) and last ($T_s = 42°C$) points as a measure of linearity.
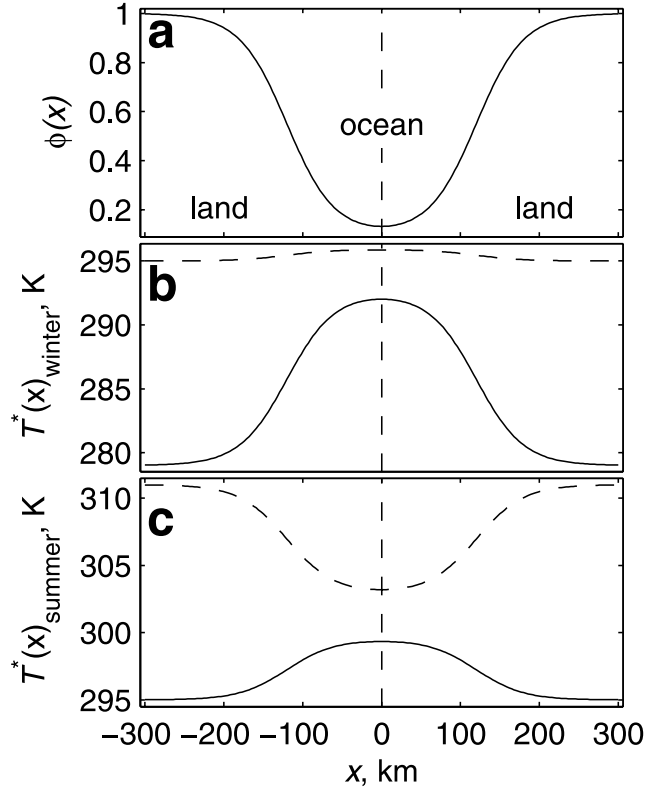
Figure 9. (a) Sructure function $\phi(x)$. Diurnal surface temperature $T_s(x)^*$ toward which the actual (b) winter and (c) summer surface temperatures of the model are relaxed.

get w_h, we employ the vertically integrated 2-D continuity equation

$$w_h = -h \frac{\partial u}{\partial x} \qquad (18)$$

with $u = 0$ at $x = \pm 300$ km. To calculate $\theta_h \equiv T_h[p_s(x, t)/p_h]^{R/cp}$, we use $T_h(x, t) = T_s(x, t) + \Gamma h$, the fact that $p_h = 925$ mbar always, and $p_s(x, t)$ from equation (12).

[23] The momentum equations are

$$\frac{\partial u}{\partial t} = fv - u \frac{\partial u}{\partial x} + \kappa \frac{\partial^2 u}{\partial x^2} - \frac{1}{2\tilde{\rho}} \frac{\partial p_s}{\partial x} \qquad (19)$$

$$\frac{\partial v}{\partial t} = -fu - u \frac{\partial v}{\partial x} + \kappa \frac{\partial^2 v}{\partial x^2} \qquad (20)$$

where $f = f(26°N)$ is the Coriolis parameter, assumed fixed because the small latitudinal extent of the domain, and vertical momentum flux is neglected.

[24] Equations (19) and (20), along with equation (10) to calculate $\tilde{\rho}$ in equation (19), equation (12) to calculate p_s in equation (10), and equation (15) with $T_h = T_s + \Gamma h$, form the closed set that is the model. We solve the model equations numerically using a third-order Adams Bashforth time scheme, 1 km spatial resolution, and no flux and flow boundary conditions at $x = \pm 300$ km. While simple, the model

is inherently nonlinear; thermal gradients force flows which, in turn, redistribute heat and modify the thermal gradients.

6. Summer Model Results

[25] Figure 10 summarizes the summer model results for 3:00 A.M. (left) and 3:00 P.M. (right). Figure 11 presents schematically the main elements of the daytime summer flow.

[26] Figures 10a and 10b show the surface temperature. In the absence of heat redistribution by flow, $T_s = T^*(x)$ should hold. The deviation, $T_s - T^*$ (the difference between the two line types in Figures 10a and 10b) reflects the dynamic heat redistribution. At the channel axis ($x = 0$), $\Delta T_{s0}^{night} \approx -0.9$ K and $\Delta T_{s0}^d \approx 1.6$ K.

[27] During the day, when surface temperatures over land far exceed those over the ocean (Figure 10b), surface pressure is maximized at the ocean's axis, and decreases away from it, attaining domain minima over neighboring land. The night configuration (Figure 10a) is reversed and has a lower amplitude. The strongest flows balancing these pressure gradients are along channel winds (i.e., in the direction consistent with geostrophy, the thin solid curves in Figures 10c and 10d; $|v|_{max} \approx 0.34$ m s^{-1}). However, because in the model formulation we exclude variability in y (along the channel, an approximation to which the Red Sea lends itself rather well), these geostrophic flows do not affect the heat or humidity budgets. At the same time, there is considerable residual ageostrophic cross-channel flow ($|u|_{max} \approx 0.07$ m s^{-1}), from the adjacent deserts toward the ocean at night (thick curve in Figure 10c), and from the ocean toward the neighboring deserts during the day (thick curve in Figure 10d). While in Figures 10c and 10d, u appears small because of the high values of v, u, and especially $\partial_x u$, are important, as described below. Over the channel axis ($x = 0$), these cross-channel flows, shown by the thick curves in Figures 10c and 10d, are strongly divergent (convergent) during the day (night). This is crucially important, as the divergence yields exceptionally strong vertical motions (Figures 10e and 10f), and related heating by vertical advective heat flux divergence (Figures 10g and 10h). Figures 10i and 10j show that lateral advective heat flux divergence, while modest compared with the vertical term (Figures 10g and 10h), cools the coasts substantially throughout the diurnal cycle, but vanishes along the channel axis.

[28] The existence of a circulation pattern similar to the one described above, with convergent (divergent) cross-channel flow during the night (day), is suggested by observations. Figure 12a shows very weakly negative sensible surface heat fluxes across the sea surface during summer in both the reanalysis [*Kalnay et al.*, 1996] and *da Silva et al.* [1994] data sets. These downward heat fluxes over the ocean are embedded in a field of otherwise strong atmospheric heating by upward surface sensible heat flux in adjacent landmasses to the east and west. Figure 12b shows that the strong heating at the lower boundary over land is accompanied by strong ascent ($\omega < 0$), while in the vicinity of the NRS the weak cooling at the lower boundary is accompanied by subsidence ($\omega > 0$). The imperfect spatial
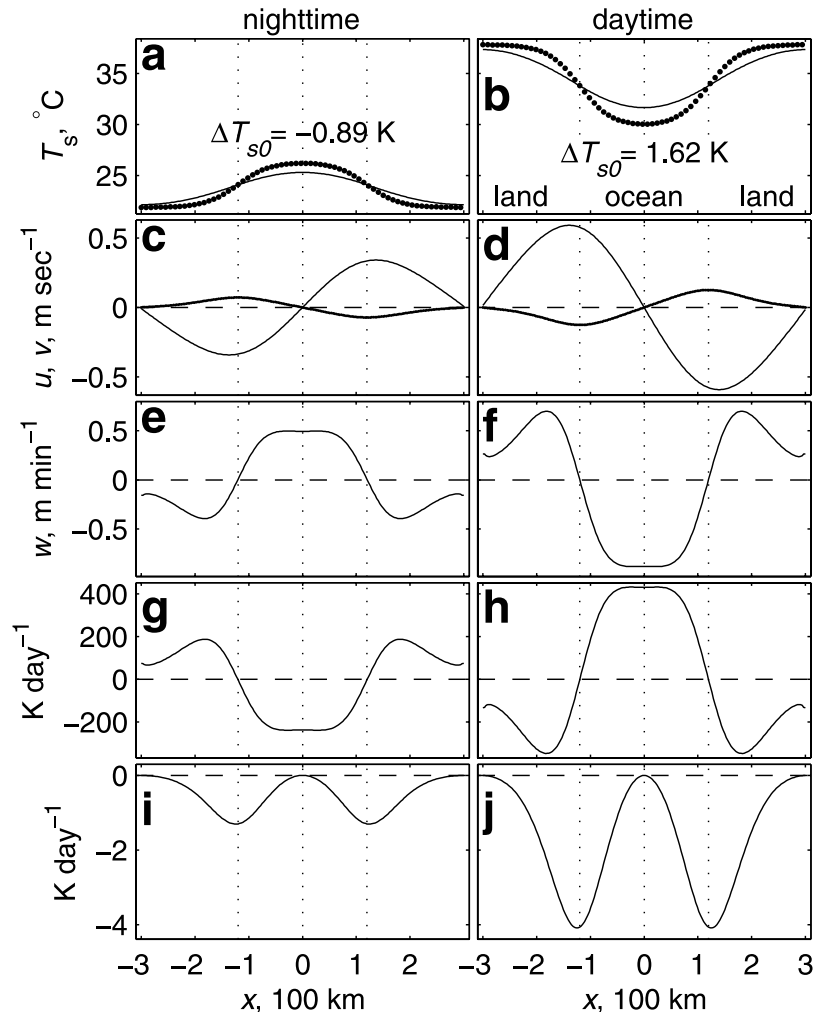
Figure 10. Results of the simple model described in text. (left) Nighttime and (right) daytime equilibrium solution. (a and b) Actual $T_s(x)$ (solid curves) and the $T^*(x)$ to which the thermal state is relaxed (dotted curves). (c–f) Flow components in the stated units. Heating in K d^{-1} due to (g and h) vertical and (i and j) lateral advective heat flux divergence, $-u\partial_x T_s$ $(-w_h\theta_h/h)$.

coincidence of the minimum heating and the maximum subsidence is expected given that the the NRS is already in the westerly wind regime, and that the atmosphere adjusts to the spatially variable heating on the deformation scale. It is easy to fill in the unobserved (at least in data arising from time averaging or smoothing) fine-scale detail, with divergent low-level lateral flows (from the ocean toward the surrounding land masses) balanced by the subsidence over the NRS shown in Figure 12b, and return flow further aloft from the surrounding hot deserts toward the ocean, fed by ascent over land.

[29] The exact magnitude of the model results, and especially the warming by vertical advective heat flux divergence (Figures 10g and 10h) should not be interpreted literally, because the model is highly idealized, and various parameters are weakly constrained by data. However, our calculations clearly demonstrate the ability of sea breezes that develop in the NRS region because of steep lateral thermal gradients to substantially affect the thermodynamics of the oceanic boundary layer.

7. Summer Subsidence Effects on Boundary Layer Humidity

[30] The summer daytime subsidence over the channel axis associated with the sea breeze flow affects evaporation in two ways. First, because of the Clausius-Clapeyron relation, the warming (Figures 10g and 10h) suppresses relative humidity for a fixed q. In addition, because $\partial_p q > 0$, subsidence tends to enhance evaporation also by suppressing BL q through downward advection of low-q air from aloft.

[31] To estimate the evaporative effect of the subsidence mediated adiabatic BL warming (i.e., addressing only the first of the above two), consider a BL with mean pressure and specific humidity of 950 mbar and 16 g kg^{-1}, characteristic of the NRS in summer. As mentioned earlier, the temperature difference at $x = 0$ between the two curves in
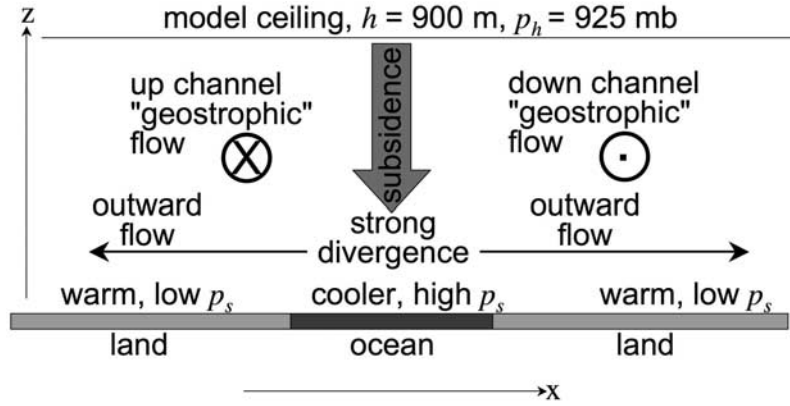
Figure 11. Schematic representation of the model daytime summer results.

Figure 10b is $\Delta T_{s0}^{d} \approx 1.6$ K. Using a traditional bulk evaporation formula,

$$E = c_e \|\mathbf{u}\| [q_s(T_s) - q], \qquad (21)$$

[e.g., *Seager et al.*, 1995; *Zhang*, 1997] where $c_e = 1.2 \times 10^{-3}$ is a dimensionless transfer coefficient, $\|\mathbf{u}\|$ is wind speed and q_s is the saturation specific humidity at the sea surface temperature, and holding wind speed fixed, the effect of the subsidence warming from 302 K to 303.6 K on evaporation is approximated as

$$\delta E^{\mathrm{day}} \stackrel{\mathrm{def}}{=} \frac{E(303.6 \mathrm{\ K})}{E(302 \mathrm{\ K})} = \frac{q_s(303.6 \mathrm{\ K}) - q}{q_s(302 \mathrm{\ K}) - q} \approx 1.25, \quad (22)$$

i.e., a 25% evaporation increase.

[32] During the night (Figure 10a), heat redistribution by the dynamics cools the model surface from 300 to 299.1 K. This cooling results in evaporation change of

$$\delta E^{\mathrm{night}} = \frac{E(299.1 \mathrm{\ K})}{E(300 \mathrm{\ K})} \approx 0.84, \qquad (23)$$

i.e., an 16% decrease.

[33] Importantly, while opposite, the day and night evaporation changes in response to subsidence warming do not cancel out. First, summer nights are obviously shorter than summer days. Even disregarding this simple fact, while nighttime evaporation reduction is 16%, daytime evaporation increase, 25%, is ~1.5 times as large. Thus averaged over the diurnal cycle, heat redistribution by the dynamics clearly enhances overall evaporation.

[34] The second way the sea breeze circulation affects the NRS BL humidity budget is through subgrid-scale (lateral and vertical) advective moisture flux divergence. To estimate these effects, we need to establish the lateral and vertical distribution of humidity, and its diurnal variability. Both are given by Figure 13. Figure 13 makes clear that the lateral variability at the two shown pressure levels (the vertical range of the curves, or even their variance bars) is small compared to the difference between either one of these levels and the surface (the gap between the curves and the circles). This is true even for 1000 mbar, a level low enough in the atmosphere to be clearly affected by the

presence of a humidity source (the ocean) immediately underneath. Therefore the lateral contribution to $-\nabla_3 \cdot \left(\overline{\mathbf{V}_3' q} \right), -\nabla_2 \cdot \left(\overline{\mathbf{V}_2' q} \right)$, must be much smaller than the vertical one, and, in geometrical height coordinate z in which the vertical velocity is w, $-\nabla_3 \cdot \left(\overline{\mathbf{V}_3' q} \right) \approx -\overline{w' \partial_z q}$ (which does not vanish in general because overbars denote averaging in time or space, and deviations from those averages may not vanish locally). Consequently, an estimate of daytime drying by the sea breeze flow, mostly subsidence that is assumed to take place somewhere between the surface and 850 mbar, is

$$\nabla_3 \cdot \left(\overline{\mathbf{V}_3' q} \right) \approx \overline{w' \partial_z \bar{q}}$$
$$\approx \overline{w_h' \left(\frac{\bar{q}_{850} - \bar{q}_{\mathrm{surface}}}{\bar{Z}_{850}} \right)}$$
$$= -1300 \mathrm{\ m \ d}^{-1} \left(\frac{5 \mathrm{\ g \ kg}^{-1} - 19 \mathrm{\ g \ kg}^{-1}}{1500 \mathrm{\ m}} \right)$$
$$\approx 12 \mathrm{\ g \ kg}^{-1} \mathrm{\ d}^{-1} \qquad (24)$$
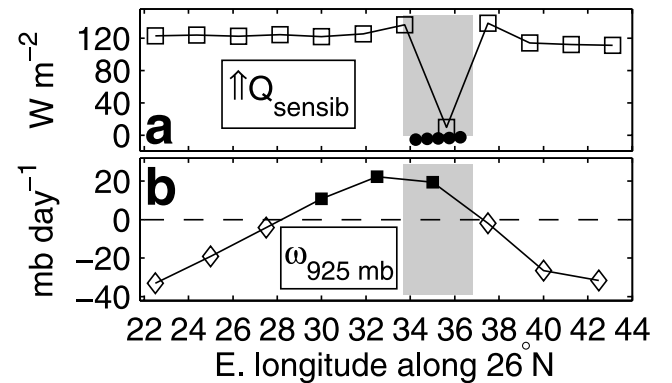
Figure 12. June–August climatologies of (a) sensible upward surface heat flux (W m^{-2}) and (b) 925 mbar subsidence (mbar d^{-1}) as a function of longitude along 26°N. In Figure 12b, squares indicate positive values. Data are from *Kalnay et al.* [1996] except the circles in Figure 12a, which are monthly mean $0.5° \times 0.5°$ climatologies from *da Silva et al.* [1994]. The approximate longitudinal extent of the Red Sea at ~26°N is shaded.
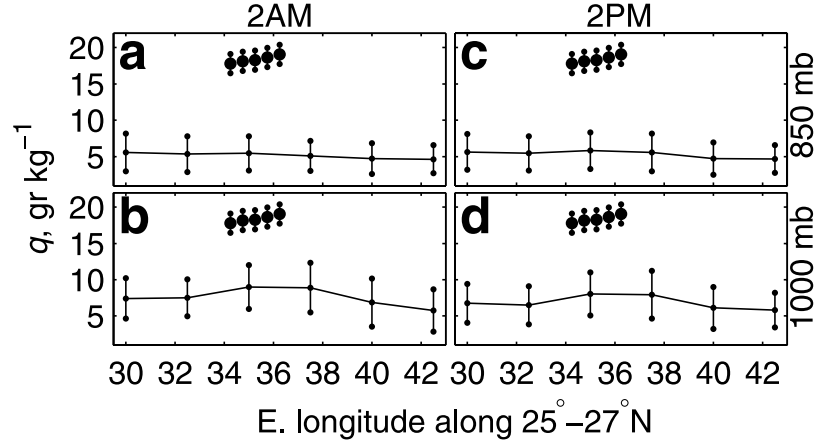
Figure 13. June–August climatologies of specific humidity as a function of longitude, averaged over 25°–27°N, at (top) 850 mbar and (bottom) 1000 mbar. Curves show climatological means of 6-hourly *Kalnay et al.* [1996] data at 0000 and 1200 UT (2:00 A.M. and 2:00 P.M. local time). Vertical solid-dotted bars show ±1.96 daily standard deviation regions about the means (curves), calculated over the 5244 time points available over 1948–2004. Circles indicate *da Silva et al.* [1994] ship-based 0.5° × 0.5° monthly mean climatologies, with monthly anomaly variability range shown by vertical bars crossing the circles.

where we use the model's $w_h \approx -0.9$ m min^{-1} $\approx$ -1300 m d^{-1} (Figure 10f) to estimate the relevant w', Figure 13 to obtain q_{850} and q_{surface}, and the reanalysis climatological NRS JJA mean 850 mbar geopotential height to estimate Z_{850}. This analysis substantiates the approximate NRS moisture budget given by equation (8), where the Reynolds term is understood to stand for "drying by diurnally varying subsidence associated with sea breeze."

[35] While the exact value of either term in equation (8) may change somewhat with alternative choices of scales or physical assumptions, it is clear that equation (8), or more specifically its more narrowly defined version

$$\overline{w'_h \partial_z \overline{q}} = \frac{\overline{E\rho_w}}{h\rho_a}, \tag{25}$$

is clearly the only viable approximation to the full moisture budget, equation (1). The validity of approximation (25), in contrast to the failure of equation (1), emphasizes the importance to the NRS BL moisture budget of subsidence drying. Importantly, the drying is achieved not by the monthly mean circulation, but by diurnally varying subsidence associated with the secondary sea breeze circulation. The validity of (25) indicates that the main reason evaporation is as high as it is in the northern Red Sea is the low boundary layer relative humidity. This low relative humidity is maintained in the presence of strong evaporative moistening by intense low-level daytime subsidence, accompanied by efficient lateral moisture evacuation near the surface that is permitted by the narrow extent of the channel. In turn, the subsidence, which overwhelms the reverse nighttime circulation, can be readily traced back to the steep spatial gradients present in the region because of the widely disparate heat capacities of the oceanic Red Sea environment and the neighboring deserts.

[36] Consistent with our earlier assertion (which led to the approximation $-\nabla_3 \cdot \left(\overline{\mathbf{V}'_3 q}\right) \approx -\overline{w' \partial_z q}$ invoked above), the lateral advective moisture flux divergence term is much smaller than its vertical counterpart;

$$\nabla_2 \cdot \langle \overline{\mathbf{V}'_2 q} \rangle \approx u'^{\text{model}}_{\text{coast}} \frac{\overline{q}_{\text{axis}} - \overline{q}_{\text{desert}}}{100 \text{ km}}$$

$$\approx 0.12 \frac{\text{m}}{\text{sec}}$$

$$\cdot \left[\frac{\frac{1}{2}(19 + 9) \text{ g kg}^{-1} - \frac{1}{2}(7 + 5) \text{ g kg}^{-1}}{100 \text{ km}} \right]$$

$$\leq 1 \text{ g kg}^{-1} \text{ d}^{-1} \tag{26}$$

where angled brackets denote vertical averaging between the surface and h (approximated as the simple arithmetic mean of the surface and 850 mbar values), and in which the short spatial length scale is chosen to render the estimate an upper bound. While lateral advective moisture flux divergence is small, the horizontal flow is still very important; it is the principal means of satisfying air mass and moisture BL continuity, and, most importantly, its divergence is what gives rise to the subsidence in the first place.

8. Winter Model Results

[37] Figure 14 is the winter counterpart of Figure 10, summarizing the winter model results for 3:00 A.M. (left) and 3:00 P.M. (right).

[38] Other than the temperatures themselves, a key difference from the summer state is that in winter, land temperatures are lower then those of the ocean throughout the diurnal cycle. While during the day surface temperatures are weakly x-dependent, land-ocean thermal contrasts are
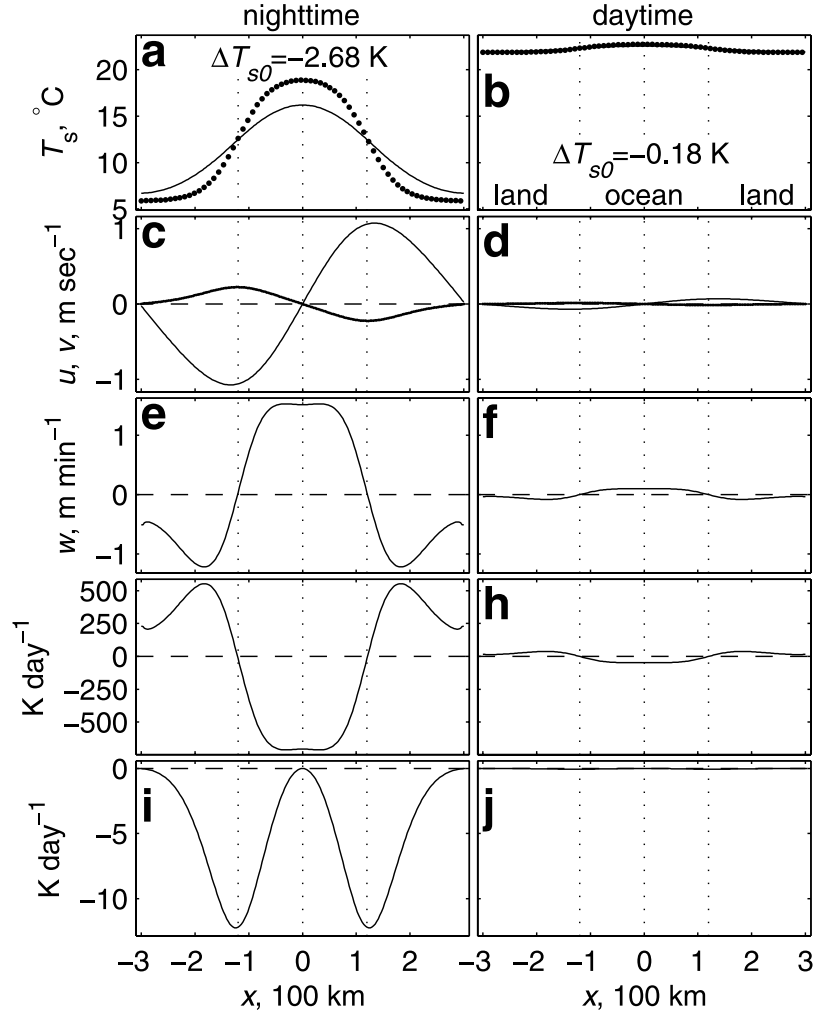
Figure 14. Results of the winter model described, following the same convention as Figure 10.

very pronounced at night, resulting in vigorous circulation. Fast and strongly convergent cross channel flows (thick curve in Figure 14c) result in strong ascent over the ocean (Figure 14e). Unlike summer, the pattern weakens, but does not change sign, during the day.

[39] The main effect of the ascent associated with this convergent surface flow pattern is estimated using Figure 15 and a modification of equation (24) appropriate for ascent,

$$\nabla_3 \cdot \left(\overline{\mathbf{V}_3' q}\right) \approx \frac{\overline{w_h' \overline{q}_h}}{h}, \qquad (27)$$

because in this configuration the motion is directed from the BL, the q of which we are interested in, into the free troposphere, the q budget of which is currently of no interest. As before, we use the model $w_h \approx 0.025 \text{ m s}^{-1} \approx 2160 \text{ m d}^{-1}$ to approximate w' at h. To obtain the advectively relevant humidity, we use the reanalysis (see Figure 15) to get $\overline{q}_{850} = 3.6 \text{ g kg}^{-1}$ and the work of *da Silva et al.* [1994] to get

$\overline{q}_{\text{surface}} = 10.3 \text{ g kg}^{-1}$, and linearly interpolate, taking $Z_{850} = 1500 \text{ m}$, between these values, to obtain $\overline{q}_{300 \text{ m}} \approx 9 \text{ g kg}^{-1}$. With these values, equation (27) yields

$$\nabla_3 \cdot \left(\overline{\mathbf{V}_3' q}\right) \approx 65 \text{ g kg}^{-1} \text{ d}^{-1}. \qquad (28)$$

This is more than enough to balance evaporative moistening, which we estimated in section 3 to be roughly 26 g kg^{-1} d^{-1}. The factor of ~2 disparity is to be expected given the model simplicity, the substantial uncertainty in our E and h estimates, and the neglect of both precipitation (which is observed, albeit minutely, in winter, and which is made more probable by the ascent) and lateral moisture delivery into the NRS BL by the convergent cross channel flows. This disparity should not obscure the main findings of this section: (1) In winter, nighttime is most relevant to the moisture budget, and (2) during winter nighttime, BL drying occurs through upward advective
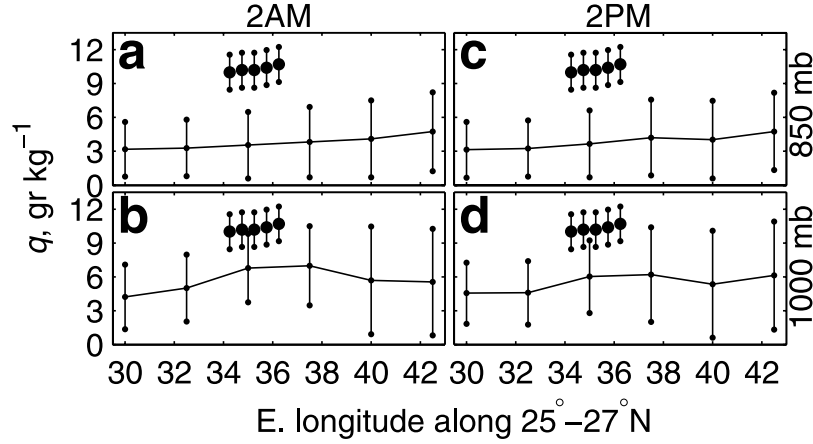
Figure 15. December–February climatologies of specific humidity as a function of longitude, averaged over 25°–27°N, at (top) 850 mbar and (bottom) 1000 mbar. Curves show climatological means of 6-hourly *Kalnay et al.* [1996] data at 0000 and 1200 UT (2:00 A.M. and 2:00 P.M. local time). Vertical solid-dotted bars show ±1.96 daily standard deviation regions about the means (curves), calculated over the 5244 time points available over 1948–2004. Circles indicate *da Silva et al.* [1994] ship-based 0.5° × 0.5° monthly mean climatologies, with monthly anomaly variability range shown by vertical bars crossing the circles.

moisture transport across the BL top by ascent that results from the convergent lateral flows.

9. Paleoclimate Implications

[40] The key ingredient to the flow patterns discussed in earlier sections of this paper is land-ocean temperature gradient. Such gradients, in the NRS as well as along other low-latitude coasts, are affected by several fundamental parameters of the climate system, such as atmospheric concentrations of greenhouse gases, the orbitally controlled insolation distribution among the seasons, the global mean solar flux, among others. We address those topics more thoroughly elsewhere (G. Eshel, The response of low-latitude coastal boundary layers to insolation changes, manuscript in preparation, 2007). In this section, however, we introduce some of the preliminaries necessary for our future in depth analysis.

[41] Qualitatively, the stronger summer insolation is, the stronger land-sea thermal contrasts, thermal gradients, and therefore cross channel flows, subsidence and evaporation, are. Conversely, the higher greenhouse gas concentrations are, the weaker winter land-sea thermal contrasts and low-level convergence into the Red Sea from the adjacent deserts are, and the weaker evaporation is.

[42] To quantitatively characterize land-sea temperature gradient, consider a surface layer of thickness ζ, heat capacity c_p and density ρ, subject to insolation flux Q_{solar}. The induced tendency of the (assumed homogeneous throughout ζ) temperature is

$$\frac{\partial T}{\partial t} = \frac{Q_{\text{solar}}}{\rho c_p \zeta} \qquad (29)$$

Considering next the NRS, the evolution of land-sea temperature difference $\delta T \equiv T^l - T^o$, in which superscripts l and o denote "land" and "ocean", is governed by

$$\frac{\partial \delta T}{\partial t} = \frac{Q_{\text{solar}}}{\rho^l c_p^l \zeta^l} - \frac{Q_{\text{solar}}}{\rho^o c_p^o \zeta^o}. \qquad (30)$$

Considering the summer daytime example, reasonable values representative of the NRS are: $Q_{\text{solar}} \sim 800$ W m^{-2}, $\rho^l \sim 1600$ kg m^{-3} (characteristic of sand), $\rho^o \sim 1000$ kg m^{-3}, $c_p^l \approx 800$ J kg^{-1} K^{-1}, $c_p^o \approx 4200$ J kg^{-1} K^{-1}, $\zeta^l \sim 3$ m, and $\zeta^o \sim 50$ m. Then,

$$\frac{\partial \delta T}{\partial t} = \frac{800}{1600 \cdot 800 \cdot 3} - \frac{800}{1000 \cdot 4200 \cdot 50} \approx 0.7 \frac{\text{K}}{\text{hr}}. \qquad (31)$$

This propensity of the NRS physical system to rapidly develop thermal gradients, the driving force behind the circulation discussed above, is a linear function of insolation; given some time varying multiplicative insolation modulator α with which the actual insolation at any time is αQ_{solar},

$$\frac{\partial \delta T}{\partial t} = \alpha \ 0.7 \ \frac{\text{K}}{\text{hr}}. \qquad (32)$$

[43] The paleoclimatic scenario most pertinent to evolution of NRS physics, the varying insolation dominance over North African climate discussed by, e.g., *deMenocal* [1995, 2004] and *Gasse* [2006], lends itself well to description in terms of equation (32), especially in summer, when insolation is the central thermal driving force. We take advantage of this by repeating the model summer calculations as
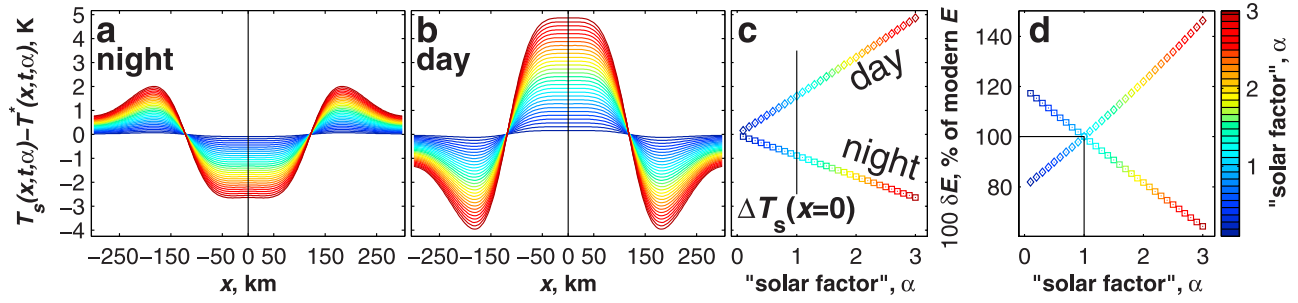
Figure 16. Sensitivity of the model summer results to the magnitude of the land-ocean thermal contrast. Full domain (-300 km $\leq x \leq 300$ km) (a) night and (b) day, $\Delta T_s(x, \alpha)$. (c) Mid channel temperature difference, $\Delta T_{s0}(\alpha)$, as a function of α. (d) The $100\delta E$ (equations (22) and (23)), the percent evaporation change relative to today's insolation. The α-dependent thermal contrast to which the model temperature equation is relaxed is given by equation (33). For each curve (Figures 16a and 16b) or symbol (Figures 16c and 16d) the color indicates the value of α, with dark blue (red) denoting $\alpha = 0.1$ ($\alpha = 3$).

described in sections 4 and 5, replacing the equation (16) summer functions with

$$T^*(x, \alpha)_{\text{nighttime}} = 300 \text{ K} - \alpha \cdot 5 \text{ K} \cdot \phi$$
$$T^*(x, \alpha)_{\text{daytime}} = 302 \text{ K} + \alpha \cdot 9 \text{ K} \cdot \phi \qquad (33)$$

with $0.1 \leq \alpha \leq 3$, i.e., exploring insolation magnitudes that give rise to NRS δT in the range of 10% to 300% of today's (with increased (decreased) insolation corresponding to $\alpha > 1$ ($\alpha < 1$)). While the extremes of this range are clearly physically implausible, we explore the stated range in order to obtain a reasonably complete picture of the dependence of NRS thermal contrasts on insolation.

[44] The results of these calculations are summarized in Figure 16. Despite the nonlinearity of the model, ΔT_{s0} scales nearly linearly with α (Figures 16a and 16b and, in particular the nearly straight lines of Figure 16c). Even when the resultant ΔT_{s0} are converted to δE (using equation (22) and the Clausius-Clapeyron relation, Figure 16d), the results are nearly linear in α despite the high-temperature nonlinearity of the Clausius-Clapeyron equation. Using Figure 16d, NRS evaporation, and thus salinity and indirectly $\delta^{18}O^{\text{water}}$, can be estimated for periods with known insolation different than today's. Since known insolation means known α, one enters the known α along the Figure 16d abscissa, and reads the resultant δE along the ordinate. Combined with today's evaporation E^{modern}, the absolute evaporation during some time τ characterized by $\alpha = \alpha^{(\tau)}$ is simply

$$E^{(\tau)} = E^{\text{modern}} \left[1 + \frac{\partial \delta E}{\partial \alpha} d\alpha \right] \qquad (34)$$

where $d\alpha \equiv \alpha - 1$ and, from Figure 16d,

$$\left. \frac{\partial \delta E}{\partial \alpha} \right|_{\text{day}} \approx \frac{1.46 - 0.81}{3 - 0} \approx 0.22 \qquad (35)$$

and

$$\left. \frac{\partial \delta E}{\partial \alpha} \right|_{\text{night}} \approx \frac{0.64 - 1.18}{3 - 0} \approx -0.18. \qquad (36)$$

[45] As an example, consider the insolation estimates of *Berger and Loutre* [1991]. They report June insolation at 30°N (a location close enough to the NRS for the purpose of this demonstration) of 474, 513 and 469 W m^{-2} currently, during the Holocene Maximum and 23 kyr, respectively. These values correspond to $\alpha = 1.08$ and 0.99 for the Holocene Maximum and 23 kyr, respectively. Using summer $E^{\text{modern}} = 1.33$ m yr^{-1}, equations (34), (35) and (36), we obtain the following summer evaporation estimates, expressed in their per year equivalents

$$E^{\text{day}}_{\text{Holoc. Max.}} = 1.33 \frac{\text{m}}{\text{yr}} [1 + 0.22 \cdot 0.08] \approx 1.35 \frac{\text{m}}{\text{yr}},$$

$$E^{\text{day}}_{\text{23 kyr}} = 1.33 \frac{\text{m}}{\text{yr}} [1 - 0.22 \cdot 0.01] \approx 1.33 \frac{\text{m}}{\text{yr}}$$

$$E^{\text{night}}_{\text{Holoc. Max.}} = 1.33 \frac{\text{m}}{\text{yr}} [1 - 0.18 \cdot 0.08] \approx 1.31 \frac{\text{m}}{\text{yr}},$$

$$E^{\text{night}}_{\text{23 kyr}} = 1.33 \frac{\text{m}}{\text{yr}} [1 + 0.18 \cdot 0.01] \approx 1.33 \frac{\text{m}}{\text{yr}}. \qquad (37)$$

Note that these calculated changes take note only of the effect of circulation mediated temperature changes, and disregard other effects, potentially larger or of the opposite sense, due to, e.g., q advection by both lateral and vertical flows or wind changes [*Rohling*, 1994]. The wind effect may well prove particularly influential, because it is multiplicative, not additive.

10. Summary and Main Conclusions

[46] In this paper, we set out to better understand the northern Red Sea climatological seasonal cycle of evaporation. We first estimated seasonal rates of boundary layer moistening by evaporation at the ocean surface, and found those rates to be of the order of 10 g kg^{-1} d^{-1} in both summer and winter. Through simple data analysis, we then demonstrated that both lateral and vertical monthly mean advective moisture flux terms are far too small to balance the evaporative moistening. This finding motivated the introduction of a simple numerical model of boundary layer

circulation in the northern Red Sea. Interpreting the model results, we concluded that the key issue in both summer and winter is the convergence/divergence patterns of cross channel ageostrophic flows that arise because of land-sea thermal contrasts.

[47] In summer, daytime is most dominant. At this time, pressure over adjacent deserts is lower than over the ocean, driving symmetric flows from the channel axis outwardly toward the neighboring deserts. These flows are strongly divergent over the ocean, resulting in subsidence. This intense subsidence dries the boundary layer both by warming it and thus reducing its relative humidity, and by introducing into the boundary layer low specific humidity air from aloft. At night the situation reverses, but because summer nights are much shorter than days, and because the nighttime flow is weaker, the above characterization holds for the summer as a whole.

[48] During winter, nighttime dominates, but the sign of the circulation is the same throughout the diurnal cycle. Cold landmasses adjacent to the northern Red Sea result in pressure gradients accelerating air from both sides of the channel toward the channel axis. The resultant surface convergence at the channel axis results in strong upward motions. The ascent dries the boundary layer by advecting upward moist boundary layer air into the free troposphere (which we crudely treat here as an infinite reservoir). Consistent with the observation that evaporation is minimized (maximized) in summer (winter), the drying processes described above are much more powerful during winter.

[49] The above results single out land-sea thermal contrasts as the main physical parameter affecting the hydrological cycle over the northern Red Sea. We conclude the paper by advancing a simple quantitative model for the response of this hydrological cycle to variable insolation fluxes which have been previously suggested as important modulators of north African climate through time. Our model results in a simple figure from which one can read the difference in northern Red Sea evaporation that is expected to characterize a known insolation change.

References

Arz, H. W., J. Patzold, P. J. Muller, and M. O. Moammar (2003), Influence of Northern Hemisphere climate and global sea level rise on the restricted Red Sea marine environment during termination I, *Paleoceanography*, *18*(2), 1053, doi:10.1029/2002PA000864.

Arz, H. W., F. Lamy, A. Ganopolski, N. Nowaczyk, and J. Patzold (2007), Dominant Northern Hemisphere climate control over millennial-scale glacial sea-level variability, *Quat. Sci. Rev.*, *26*(34), 312–321, doi:10.1016/j.quascirev.2006.07.016.

Berger, A., and M. F. Loutre (1991), Insolation values for the climate of the last 10 m.y., *Quat. Sci. Rev.*, *10*, 297–317.

Cember, R. P. (1988), On the sources, formation, and circulation of Red Sea deep water, *J. Geophys. Res.*, *93*(C7), 8175–8191.

Cember, R. P. (1989), Bomb radiocarbon in the Red Sea: A medium-scale gas exchange experiment, *J. Geophys. Res.*, *94*(C2), 2111–2123.

da Silva, A., A. C. Young, and S. Levitus (1994), *Atlas of Surface Marine Data 1994*, vol. 1, *Algorithms and Procedures, NOAA Atlas NES-DIS*, vol. 6, NOAA, Silver Spring, Md.

Deardroff, J. W. (1972), Parameterization of the planetary boundary layer for use in general circulation models, *Mon. Weather Rev.*, *100*, 93–106.

deMenocal, P. B. (1995), Plio-Pleistocene African climate, *Science*, *270*, 53–59.

deMenocal, P. B. (2004), African climate change and faunal evolution during the Pliocene-Pleistocene, *Earth Plant. Sci. Lett.*, *220*, 3–24.

Eshel, G., and J. J. Bernstein (2006), Relationship between large-scale atmospheric states, subsidence, static stability and ground-level ozone in Illinois, USA, *Water, Air Soil Pollut.*, *171*, 111–133.

Eshel, G., and N. Naik (1997), Climatological coastal jet collision, intermediate water formation and the general circulation of the Red Sea, *J. Phys. Oceanogr.*, *27*, 1233–1257.

Eshel, G., D. P. Schrag, and B. F. Farrell (2000), Troposphere–planetary boundary layer interactions and the evolution of ocean surface density: Lessons from Red Sea corals, *J. Clim.*, *13*, 339–351.

Gasse, F. (2006), Climate and hydrological changes in tropical Africa during the past million years, *C. R. Palevol.*, *5*, 35–43.

Genin, A., B. Lazar, and S. Brenner (2002), Vertical mixing and coral death in the Red Sea following the eruption of Mount Pinatubo, *Nature*, *377*, 507–510.

Holstlag, A. A. M., and C.-H. Moeng (1991), Eddy diffusivity and countergradient transport in the convective atmospheric boundary layer, *J. Atmos. Sci.*, *48*, 1690–1698.

Jones, P. D., and A. Moberg (2003), Hemispheric and large-scale surface air temperature variations: An extensive revision and an update to 2001, *J. Clim.*, *16*, 206–223.

Kalnay, E., et al. (1996), The NCEP/NCAR 40–Year Reanalysis Project, *Bull. Am. Meteorol. Soc.*, *77*, 437–472.

Morcos, S. A. (1970), Physical and chemical oceanography of the Red Sea, *Oceanogr. Mar. Biol.*, *8*, 73–202.

New, M. G., M. Hulme, and P. D. Jones (2000), Representing twentieth-century space-time climate variability. part II: Development of 1901–1996 monthly grids of terrestrial surface climate, *J. Clim.*, *13*, 2217–2238.

Rohling, E. J. (1994), Glacial conditions in the Red Sea, *Paleoceanography*, *9*, 653–660.

Rohling, E. J., M. Fenton, F. J. Jorissen, P. Bertrand, G. Ganssen, and J. P. Caulet (1998), Magnitudes of sea-level lowstands of the past 500,000 years, *Nature*, *394*, 162–165.

Seager, R., M. B. Blumenthal, and Y. Kushnir (1995), An advective atmospheric mixed layer model for ocean modeling purposes: Global simulation of surface heat fluxes, *J. Clim.*, *8*, 1951–1964.

Siddall, M., E. J. Rohling, A. Almogi-Labin, C. Hemleben, D. Meischner, I. Schmelzer, and D. A. Smeed (2003), Sea-level fluctuations during the last glacial cycle, *Nature*, *423*, 853–858.

Sirocko, F. (2003), Ups and downs in the Red Sea, *Nature*, *423*, 813–814.

Smeed, D. A. (2004), Exchange through the Bab el Mandab, *Deep Sea Res., Part II*, *51*, 455–474.

Sobel, A. H. (2003), On the coexistence of an evaporation minimum and precipitation maximum in the Warm Pool, *J. Clim.*, *16*, 1003–1009.

Sofianos, S. S., W. E. Johns, and S. P. Murray (2002), Heat and freshwater budgets in the Red Sea from direct observations at Bab el Mandeb, *Deep Sea Res., Part II*, *49*, 1323–1340.

Thunell, R. C., S. E. Locke, and D. F. Williams (1988), Glacio-eustatic control on Red Sea salinity, *Nature*, *334*, 601–604.

Tragou, E., C. Garrett, R. Outerbridge, and C. Gilman (1999), The heat and freshwater budgets of the Red Sea, *J. Phys. Oceanogr.*, *29*, 2504–2522.

Vogelezang, D. H. P., and A. A. M. Holtslag (1996), Evaluation and model impacts of alternative boundary-layer height formulations, *Boundary Layer Meteorol.*, *81*, 245–269.

Zhang, G. J. (1997), A further study on estimating surface evaporation using monthly mean data: Comparison of bulk formulations, *J. Clim.*, *10*, 1592–1600.

————————

G. Eshel, Division of Science, Mathematics and Computing, Simon's Rock College of Bard, 84 Alford Road, Great Barrington, MA 01230, USA. (geshel@simons-rock.edu)

N. Heavens, Division of Geological and Planetary Sciences, California Institute of Technology, 1200 E. California Blvd., Pasadena, CA 91125, USA.